hv photonics

IMPACT FACTOR 2.1

CITESCORE 2.6

Communication

Probing *nS*/*nD* Rydberg States via $6P_{3/2}$ Intermediate Level Using Electromagnetically Induced Transparency in ^{87}Rb

Donghao Li, Beining Xu, Keyu Qin, Xin Jia, Changtao Zhao, Yaoting Zhou and Zhongxiao Xu

MDPI

https://doi.org/10.3390/photonics12030204

photonics

MDPI

Communication

Probing nS/nD Rydberg States via $6P_{3/2}$ Intermediate Level Using Electromagnetically Induced Transparency in ^{87}Rb

Donghao Li [1,2], Beining Xu [1], Keyu Qin [1], Xin Jia [1], Changtao Zhao [1], Yaoting Zhou [1] and Zhongxiao Xu [1,2,*]

[1] State Key Laboratory of Quantum Optics Technologies and Devices, Institute of Opto-Electronics, Shanxi University, Taiyuan 030006, China; lidonghao@sxu.edu.cn (D.L.)
[2] Collaborative Innovation Center of Extreme Optics, Shanxi University, Taiyuan 030006, China
* Correspondence: xuzhongxiao@sxu.edu.cn

Abstract: We perform precise measurements of the ^{87}Rb Rydberg excitation spectrum by using electromagnetically induced transparency (EIT) in a ladder system. We utilize a two-photon excitation configuration with the probe and control lasers at 420 nm and 1013 nm, respectively. In this work, we employ $6P_{3/2}, F^{'} = 3$ as an intermediate state to excite the high-lying Rydberg states of the nS and nD series, with principal quantum numbers ranging from $n = 35$ to $n = 70$. To improve the signal-to-noise ratio (SNR) in this inverted level scheme ($\lambda_p < \lambda_c$), we apply a 100 kHz chopping to the control beam, which is followed by a demodulation operated with a lock-in amplifier. Additionally, we verify the ionization energies and determine the quantum defects for the nS and nD series, respectively. Our work offers a database for applications of large-scale quantum simulation and quantum computation with the ^{87}Rb atom array.

Keywords: inverted two-photon Rydberg excitation; electromagnetically induced transparency; ionization energy; quantum defect

1. Introduction

The array of neutral atoms emerges as an ideal platform for large-scale quantum computation and simulation [1–5], attributed to their reconfigurable geometries [6,7], single-atom addressability [8], and arbitrary connectivity [9]. Central to this system is the excitation of Rydberg states [10]. Rydberg atoms, being in a highly excited state, exhibit a significant increase in atomic electric dipole moment, leading to long-range interactions that can extend over micrometer scales. This provides a powerful tool for implementing two-qubit entangled gates in quantum circuits [11–13] and exploring interacting many-body dynamics [14–16] and quantum phase [17].

Conventionally, a two-photon excitation associated with transitions $5S_{1/2} \rightarrow 5P_{3/2} \rightarrow nS/nD$ is applied to prepare the Rydberg states of ^{87}Rb atoms, wherein lasers at 780 nm and 480 nm are used. Consequently, the Rydberg excitation of neutral atoms in large-scale arrays necessitates substantial laser power at 480 nm, due to the scaling of power requirements with array size. In practice, the generation of the 480 nm-laser is based on frequency doubling. However, the limited seeds power and low conversion efficiency, due to serious absorption and the heating effect with blue light, impede the production of the high-power 480 nm laser. To address this issue, the inverted scheme of two-photon excitation was proposed, involving the transitions $5S_{1/2} \rightarrow 6P_{3/2} \rightarrow nS/nD$ driven by 420 nm and 1013 nm lasers [18]. In this case, the requirement of the high-power 1013 nm laser can be fulfilled by using a doped fiber amplifier. Yet, the data associated with this

check for updates

Received: 23 January 2025
Revised: 15 February 2025
Accepted: 25 February 2025
Published: 26 February 2025

Citation: Li, D.; Xu, B.; Qin, K.; Jia, X.; Zhao, C.; Zhou, Y.; Xu, Z. Probing nS/nD Rydberg States via $6P_{3/2}$ Intermediate Level Using Electromagnetically Induced Transparency in ^{87}Rb. *Photonics* **2025**, *12*, 204. https://doi.org/10.3390/photonics12030204

transition has never been reported in any publications. In particular, the poor signal-to-noise ratio (SNR) of the corresponding electromagnetically induced transparency (EIT) spectrum further restricts the laser frequency reference in such an inverted configuration.

In this study, we investigate the Rydberg excitation spectrum with the 420 nm–1013 nm two-photon transition in hot ^{87}Rb atomic vapor. Concretely, the ladder-type EIT is utilized to illustrate the excitation, and we use $6P_{3/2}$ as the intermediate state. Here, the 420 nm (λ_p) laser is emitted by a frequency doubler with the seeds from a Ti:sapphire laser, while the external cavity diode laser (ECDL) provides a frequency tunable 1013 nm (λ_c) laser for fiber optic amplification, enabling the EIT spectrum scanning. Furthermore, we leverage a modulation–demodulation protocol to obtain the high-performance EIT spectrum with principal quantum numbers ranging from $n = 35$ to $n = 70$. In combination with the ionization energy calculation, our result thus provides the full information of 420 nm–1013 nm two-photon Rydberg excitation, which can be directly applied to scalable quantum information processing with ^{87}Rb atoms.

2. Experimental Setup

The schematic of EIT measurement is outlined in Figure 1. Our experiment is performed with an isotopically enriched ^{87}Rb vapor cell maintained at the operation temperature of 60 °C. This cylindrical cell, with diameter of 2.5 cm and length of 7.5 cm, resides inside a single-layer magnetic shielding to screen out the ambient magnetic field.

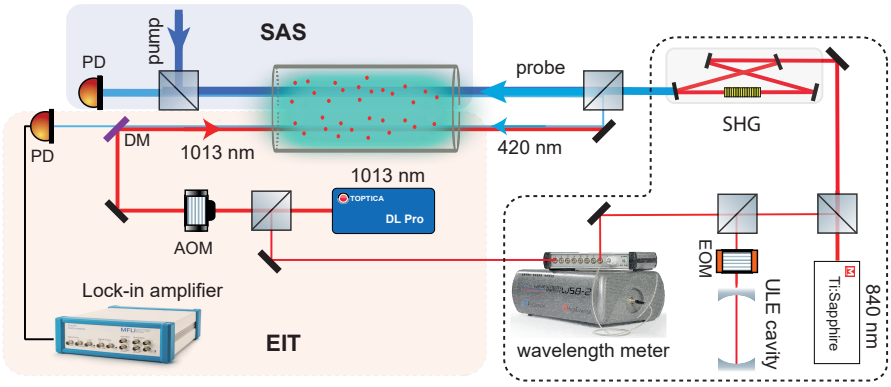

Figure 1. Schematic of the experimental setup for Rydberg excitation spectrum measurement in ^{87}Rb atomic vapor. A Ti:Sapphire laser operating at 840 nm is frequency-doubled to generate the 420 nm light. The 840 nm seed laser is locked to an ultra-low expansion (ULE) cavity, overcoming the frequency drift caused by temperature variation. A small portion of the 420 nm is used for saturated absorption spectroscopy (SAS). By tuning the sideband frequency, the 420 nm laser can be scanned. The 1013 nm laser is produced by a Toptica laser and counter-propagated with the 420 nm laser for realizing the Rydberg spectrum measurement. An acoustic optical modulator (AOM) is employed for chopping the 1013 nm light. The transmitted 420 nm passes through the dichroic mirror (DM) and is sent to a lock-in amplifier to extract the weak EIT signal. A wavelength meter (Highfinesse, WS8-2) continuously monitors the frequencies of all lasers. The vapor cell, 7.5 cm in length and 2.5 cm in diameter, is heated to 60 °C for both SAS and EIT detection. SHG: second harmonic generation, EOM: electro-optic modulator, and PD: photodetector.

In this 420 nm–1013 nm two-photon excitation scheme (Figure 2a), a 420 nm laser is generated by frequency-doubled via second harmonic generation (SHG). In order to prepare such a beam, we use a seed laser at 840 nm emitted by a frequency tunable Ti:Sapphire laser (M Square), which provides high output power and narrow linewidth light source. This seed laser is frequency-locked to an ultra-low expansion (ULE) cavity (fineness∼40,000) through the sideband Pound-Drever-Hall (PDH) locking technique, ensuring the SHG-generated 420 nm laser is resonant to the transition between $5S_{1/2}, F = 2$ and $6P_{3/2}, F^{'} = 3$

of ^{87}Rb atoms. In experiments, we expand the beam size to 4 mm in diameter by utilizing a pair of plano-convex lenses, and we set the power ratio of the probe to pump beams to approximately 1:10 to enhance the SAS signal [19]. The associated result of saturated absorption spectroscopy (SAS) is displayed in Figure 2b.

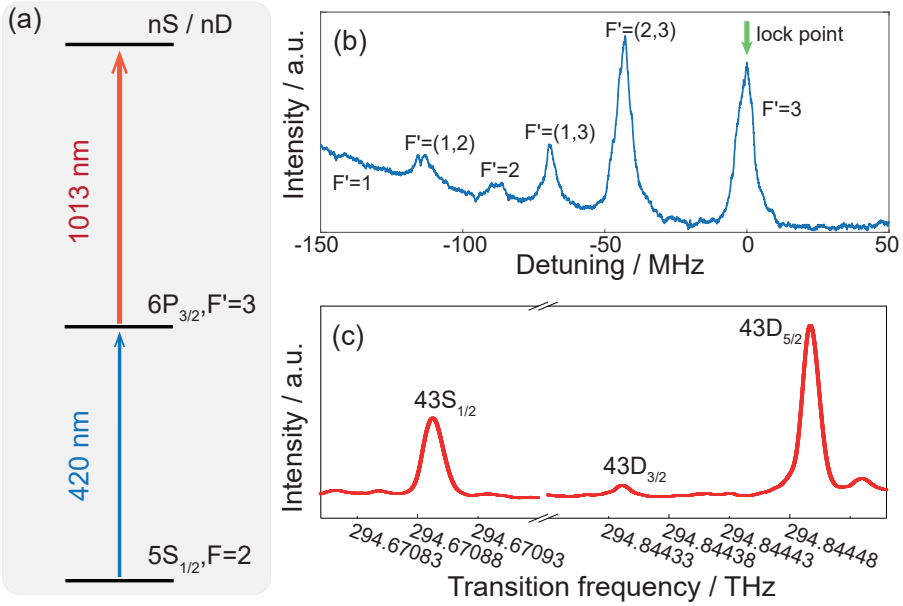

Figure 2. (**a**) Energy−level diagram of Rydberg excitation via two-photon transitions. (**b**) SAS of the $5S_{1/2}, F = 2$ to $6P_{3/2}, F^{'} = 3$ at 420 nm. The peak of $F^{'} = (m, n)$ corresponds to the crossover resonance peak resulting from the $F^{'} = m$ and $F^{'} = n$ peaks. (**c**) Recorded EIT signals for the $6P_{3/2}$ to $nS_{1/2}$, $nD_{3/2}$, and $nD_{5/2}$ transitions at the principal quantum number $n = 43$, showcasing the characteristic transparency peaks associated with each state.

The control light at 1013 nm driving the transition $6P_{3/2}, F^{'} = 3$ to Rydberg state nS/nD is emitted by a ECDL (Toptica, DL pro). The counter-propagating probe (420 nm) and control (1013 nm) fields set up the Rydberg EIT process. The transmitted light of 420 nm is separated from the 1013 nm beam with a dichroic mirror (DM) and subsequently detected by a photodetector (PD). When scanning the frequency of the 1013 nm laser, i.e., single-photon detuning corresponding to the transition $6P_{3/2}, F^{'} = 3$ to the Rydberg state nS/nD, the EIT spectrum is extracted by using a lock-in amplifier with a demodulation frequency at 100 kHz. In addition, the laser frequencies of 420 nm and 1013 nm are continuously monitored by a wavelength meter (Highfinesse, WS8-2) to accurately record the two-photon transition frequencies.

3. Results

In our experiment, we adopt the configuration with $\lambda_p < \lambda_c$ to address the issue of high power requirement on the blue laser. However, in this inverted scheme, the Doppler shifts for both the one-photon, $-k_p v$, and two-photon, $-(k_p v - k_c v)$, have the same sign, and thus the transparency window vanishes [20–22]. As a consequence, given the Doppler averaged absorption, the magnitude of the EIT structure is significantly reduced by many orders with respect to the case that the probe wavelength is longer than the coupling wavelength.

In order to improve the SNR of the EIT signal, we apply a 100 kHz intensity modulation with the periodical rectangular pulses and 50% duty cycle. Meanwhile, the beam size of 420 nm is reduced to 200 µm to increase the Rabi frequency between $5S_{1/2}$ and $6P_{3/2}$. The relative frequencies for the transitions from $6P_{3/2}$ to nS and nD states are measured by scanning the 1013 nm laser.

By using this method, we investigate the spectrum of high-lying Rydberg excited states, including the nS and nD series, with principal quantum numbers ranging from $n = 35$ to $n = 70$. Figure 2c displays the EIT spectrum associated with the transition from the state $6P_{3/2}$ to Rydberg states $43S_{1/2}$ / $43D_{3/2}$ / $43D_{5/2}$. Notably, the signal associated with the $D_{5/2}$ state transitions is significantly stronger than that of the $D_{3/2}$ state transitions in the observed spectrum. The relative intensities of $nD_{3/2}$ and $nD_{5/2}$ are determined by the geometric part of the electric dipole transition matrix element.

To ensure the accuracy of our frequency measurements, we utilize a wavelength meter that is consistently calibrated in real-time using a Rubidium atomic clock (High-finesse Stabilized Laser Reference, SLR780), which is operated at 384.228115 THz. This calibration approach guarantees that our measurements are in line with the highest precision benchmarks set by atomic clock standards. The transition of $5S_{1/2}$, $F = 2 \rightarrow 6P_{3/2}, F^{'} = 3$ is observed at a frequency of 713.281710(5) THz. The value, however, exhibits a difference of 30 MHz, with the result reported in Ref. [23]. We repeat the measurement several times to obtain this resonant frequency, and the deviation is much less than the 30 MHz. It shows that a stable offset can occur when there a substantial wavelength disparity exists between the calibration laser (780 nm) and the target laser.

By fixing this resonant transition, we further measure the transition frequency from $6P_{3/2}, F^{'} = 3$ to the Rydberg state nS/nD via scanning the frequency of a 1013 nm laser. The measured transition frequencies are summarized in Table 1. In this process, the measured mean deviation of several measurements is approximately 10 MHz. Here, the external field interferenceis effectively mitigated by enclosing the vapor in a single-layer μ-metal shield, rendering its impact negligible. Thus, the main factors of measurement uncertainty are attributed to systematic vibrations, which induce spectral line shifts, and the thermal drift of the wavelength meter. Furthermore, we find that there is a significant discrepancy of approximately 300 MHz between the experimental data and the theoretical values of the transition frequency, which is larger than the measurement uncertainty (around 10 MHz). This difference primarily arises from the idealized model employed and the initial values selected for the quantum defects in ARC. The similar discrepancies have also been reported in Refs. [24,25].

Building upon the measured results, we can determine the ionization energy and quantum defect of ^{87}Rb. The ionization energy for a given Rydberg level, characterized by quantum numbers n, l, and j, is described by the following relation [26]:

$$E_{n,l,j} = E_{\infty} - E_{hfs} - \frac{R_y}{(n - \delta_{n,l,j})^2}, \quad (1)$$

where $E_{n,l,j}$ represents energy levels of the Rydberg states. The term E_{∞} denotes the ionization energy threshold. The hyperfine splitting between the ground state sublevels $5S_{1/2}, F = 1$ and $5S_{1/2}, F = 2$ is represented by E_{hfs}, and R_y =h·3289.82119466(2) THz is the Rydberg constant, corrected for the reduced electron mass in ^{87}Rb [27], where h is Planck's constant.

Table 1. Measured transition frequencies between the intermediate state $6P_{3/2}, F' = 3$ and Rydberg state nS/nD series in theory and experiment. Here, n is principal quantum number and the theoretical value of the transition is calculated by Ref. [28].

n	$nS_{1/2}$ (THz)		$nD_{3/2}$ (THz)		$nD_{5/2}$ (THz)	
	Theory	Exp	Theory	Exp	Theory	Exp
35	293.501710	293.501345(10)	293.836011	293.835671(10)	293.836291	293.835947(10)
36	293.695816	293.695414(10)	294.001250	294.000881(10)	294.001506	294.001141(10)
37	293.872984	293.872618(10)	294.152780	294.152374(10)	294.153016	294.152608(10)
38	294.035129	294.034759(10)	294.292079	294.291713(10)	294.292296	294.291928(10)
39	294.183901	294.183527(10)	294.420428	294.420057(10)	294.420627	294.420266(10)
40	294.320733	294.320351(10)	294.538944	294.538536(10)	294.539129	294.538721(10)
41	294.446868	294.446492(10)	294.648608	294.648222(10)	294.648779	294.648397(10)
42	294.563394	294.563008(10)	294.750279	294.749911(10)	294.750438	294.750079(10)
43	294.671262	294.670892(10)	294.844716	294.844341(10)	294.844864	294.844492(10)
44	294.771309	294.770909(10)	294.932589	294.932204(10)	294.932727	294.932334(10)
45	294.864273	294.863898(10)	295.014493	295.014115(10)	295.014621	295.014244(10)
46	294.950807	294.950437(10)	295.090955	295.090595(10)	295.091075	295.090708(10)
47	295.031492	295.031124(10)	295.162449	295.162065(10)	295.162561	295.162182(10)
48	295.106842	295.106471(10)	295.229394	295.229027(10)	295.229500	295.229134(10)
49	295.177317	295.176951(10)	295.292170	295.291818(10)	295.292269	295.291916(10)
50	295.243330	295.242940(10)	295.351114	295.350753(10)	295.351207	295.350842(10)
51	295.305249	295.304861(10)	295.406534	295.406158(10)	295.406621	295.406251(10)
52	295.363406	295.363035(10)	295.458703	295.458331(10)	295.458785	295.458413(10)
53	295.418100	295.417729(10)	295.507872	295.507479(10)	295.507949	295.507560(10)
54	295.469600	295.469232(10)	295.554266	295.553897(10)	295.554339	295.553972(10)
55	295.518150	295.517760(10)	295.598090	295.597706(10)	295.598159	295.597787(10)
56	295.563971	295.563609(10)	295.639531	295.639158(10)	295.639596	295.639219(10)
57	295.607264	295.606868(10)	295.678758	295.678381(10)	295.678820	295.678443(10)
58	295.648212	295.647842(10)	295.715926	295.715547(10)	295.715985	295.715607(10)
59	295.686980	295.686628(10)	295.751177	295.750806(10)	295.751232	295.750861(10)
60	295.723722	295.723339(10)	295.784640	295.784269(10)	295.784693	295.784321(10)
61	295.758575	295.758206(10)	295.816434	295.816095(10)	295.816485	295.816151(10)
62	295.791667	295.791298(10)	295.846669	295.846337(10)	295.846717	295.846385(10)
63	295.823115	295.822743(10)	295.875445	295.875142(10)	295.875490	295.875200(10)
64	295.853025	295.852633(10)	295.902854	295.902471(10)	295.902897	295.902509(10)
65	295.881497	295.881113(10)	295.928981	295.928611(10)	295.929022	295.928651(10)
66	295.908622	295.908259(10)	295.953905	295.953542(10)	295.953944	295.953581(10)
67	295.934482	295.934090(10)	295.977699	295.977379(10)	295.977737	295.977421(10)
68	295.959155	295.958781(10)	296.000430	296.000057(10)	296.000466	296.000089(10)
69	295.982713	295.982340(10)	296.022161	296.021778(10)	296.022195	296.021809(10)
70	296.005225	296.004855(10)	296.042948	296.042575(10)	296.042982	296.042611(10)

To accurately describe the quantum defects associated with the Rydberg states, we employ the Rydberg–Ritz equation [27] :

$$\delta_{n,l,j} \approx \delta_0 + \frac{\delta_2}{(n-\delta_0)^2} + \frac{\delta_4}{(n-\delta_0)^4} + \ldots \tag{2}$$

The dominant dependence of the quantum defect lies in the l, with negligible contributions from higher-order terms in j and n for Rydberg states. For the $n > 20$, we consider only the first two terms of the equation, which provides an approximation for the quantum defect. This correction accounts for deviations from the energy levels predicted by the classical calculation of the hydrogen wavefunction. Here, δ_0 and δ_2 represent fitting parameters, whose values are determined by optimizing the agreement with experimental data from Table 1 [29,30].

Figure 3 illustrates the dependence of Rydberg energy levels on the principal quantum number n, whereby the experimental data are fitted with Equation (1). These fitting results tell us that the ionization energy levelsE_∞/h for nS, $nD_{3/2}$, and $nD_{5/2}$ are 1010.0291339(12) THz, 1010.0291784(15) THz and 1010.0291709(18) THz, respectively. The value for nS states agrees well with the results in Ref. [27]. Additionally, the parameters δ_0 and δ_2 in the Rydberg–Ritz formula have been extracted from our fitting data, and the ionization energy E_∞/hc is displayed in Table 2.

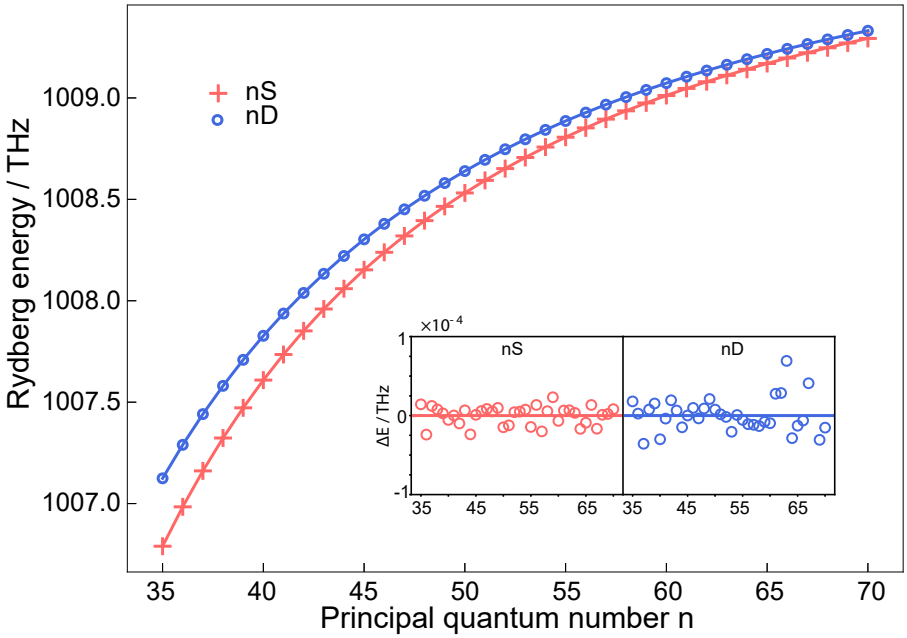

Figure 3. Energies of Rydberg states for nS (red plus) and nD (blue circle) corresponding to principal quantum numbers ranging from $n = 35$ to $n = 70$. The solid lines depict the fitted curves corresponding to nS and nD series, respectively. The insets display the difference ΔE between the data and the fit for each series. The residual squared (R^2) differs from 1 by 10^{-10} and 10^{-9} for the nS and $nD_{3/2}$ series, respectively. Here, only the $nD_{3/2}$ series is plotted, due to the small energy difference between the $nD_{3/2}$ and $nD_{5/2}$ levels.

Table 2. Determination of quantum defects δ_0 and δ_2 for the nS and nD Rydberg states of ^{87}Rb. The ionization frequency from the ground state $5S_{1/2}, F = 1$ is calculated on basis of the fit result in this work and compared with the result reported in Ref. [27].

		This Work	**Ref. [27]**
$nS_{1/2}$	δ_0	3.1311650(8)	3.1311807(8)
	δ_2	0.2119(2)	0.1787(2)
$nD_{3/2}$	δ_0	1.3493698(11)	1.3480948(11)
	δ_2	−1.8656(4)	−0.6054(4)
$nD_{5/2}$	δ_0	1.3474759(11)	1.3464622(11)
	δ_2	−1.5901(4)	−0.5940(4)
$E_{\infty,5S_{1/2},F=1}/hc$		33,690.94541(6) cm^{-1}	33,690.94644(1) cm^{-1}

4. Conclusions

We report the precise measurement of the ^{87}Rb Rydberg excitation spectrum in an inverted ladder-type EIT configuration. This setup couples the $5S_{1/2}$ ground state with the nS or nD Rydberg states via the $6P_{3/2}$ intermediate state, overcoming the shortcoming of the high power requirement in the 780 nm–480 nm two-photon excitation. Furthermore,

by using a modulation–demodulation protocol we extract the EIT features from the noisy backgrounds. Importantly, we measure the Rydberg transition frequencies for the principal quantum number $n = 35$ to $n = 70$, and we calculate the Rydberg energy. By fitting the data, we obtained the corresponding ionization energies and quantum defects. Our results provide the experimental data reference for applications on large-scale quantum information processing with ^{87}Rb Rydberg atoms and promote novel experiments related to Rydberg atoms with long-range dipole-dipole interactions.

Author Contributions: Conceptualization, D.L. and K.Q; methodology and formal analysis, D.L.; data curation, B.X.; investigation, B.X., K.Q., X.J., C.Z. and Y.Z.; writing—original draft, D.L. and B.X.; writing—review and editing, D.L. and Z.X.; experimental setup, B.X. and K.Q.; and project administration and supervision, D.L. and Z.X. All authors have read and agreed to the published version of the manuscript.

Funding: This work was funded by National Key R&D Program of China (Grant No. 2020YFA0309400), the National Natural Science Foundation of China (Grant No. 12222409, 12204289), and the Key Research and Development Program of Shanxi Province (Grant No. 202101150101025).

Institutional Review Board Statement: Not applicable.

Informed Consent Statement: Not applicable.

Data Availability Statement: The original contributions presented in the study are included in the article; further inquiries can be directed to the corresponding author.

Conflicts of Interest: The authors declare no conflicts of interest.

References

1. Bluvstein, D.; Evered, S.J.; Geim, A.A. Logical quantum processor based on reconfigurable atom arrays. *Nature* **2024**, *626*, 58–65. [CrossRef] [PubMed]
2. Henriet, L.; Beguin, L.; Signoles, A. Quantum computing with neutral atoms. *Quantum* **2020**, *4*, 327. [CrossRef]
3. Sunami, S.; Tamiya, S.; Inoue, R. Scalable Networking of Neutral-Atom Qubits: Nanofiber-Based Approach for Multiprocessor Fault-Tolerant Quantum Computer. *arXiv* **2024**, arXiv:2407.11111. [CrossRef]
4. Bornet, G.; Emperauger, G.; Chen, C. Scalable spin squeezing in a dipolar Rydberg atom array. *Nature* **2023**, *621*, 728–733. [CrossRef]
5. Scholl, P.; Schuler, M.; Williams, H.J. Quantum simulation of 2D antiferromagnets with hundreds of Rydberg atoms. *Nature* **2021**, *595*, 233–238. [CrossRef]
6. Barredo, D.; Lienhard, V.; De Leseleuc, S.; Lahaye, T.; Browaeys, A. Synthetic three-dimensional atomic structures assembled atom by atom. *Nature* **2018**, *561*,79–82. [CrossRef]
7. Maskara, N.; Ostermann, S.; Shee, J. Programmable Simulations of Molecules and Materials with Reconfigurable Quantum Processors. *arXiv* **2023**, arXiv:2312.02265. [CrossRef]
8. Endres, M.; Bernien, H.; Keesling, A. Atom-by-atom assembly of defect-free one-dimensional cold atom arrays. *Science* **2016**, *354*, 1024–1027. [CrossRef]
9. Nguyen, M.; Jin-Guo, L.; Wurtz, J. Quantum Optimization with Arbitrary Connectivity Using Rydberg Atom Arrays. *PRX Quantum* **2023**, *4*, 010316. [CrossRef]
10. Saffman, M. Quantum computing with atomic qubits and Rydberg interactions: Progress and challenges. *J. Phys. B At. Mol. Opt. Phys.* **2016**, *49*, 2020001. [CrossRef]
11. Evered, S.J.; Bluvstein, D.; Kalinowski, M. High-fidelity parallel entangling gates on a neutral-atom quantum compute. *Nature* **2023**, *622*, 268–272. [CrossRef] [PubMed]
12. Graham, T.M.; Song, Y.; Scott, J. Multi-qubit entanglement and algorithms on a neutral-atom quantum computer. *Nature* **2022**, *604*, 457–462. [CrossRef] [PubMed]
13. Crescimanna, V.; Taylor, J.; Goldberg, A.Z. Quantum Control of Rydberg Atoms for Mesoscopic Quantum State and Circuit Preparation. *Phys. Rev. Appl.* **2023**, *20*, 034019. [CrossRef]
14. Serbyn, S.; Abanin, D.A.; Papić, Z. Quantum many-body scars and weak breaking of ergodicity. *Nat. Phys.* **2021**, *17*, 675–685. [CrossRef]
15. Lee, J.Y.; Ramette, J.; Metlitski, M.A. Landau-Forbidden Quantum Criticality in Rydberg Quantum Simulators. *Phys. Rev. Lett.* **2023**, *131*, 083601. [CrossRef]

16. Browaeys, A.; Thierry, L. Many-body physics with individually controlled Rydberg atoms. *Nat. Phys.* **2020**, *16*, 132–142. [CrossRef]
17. Ebadi, S.; Wang, T.T.; Ha Levine, A. Quantum phases of matter on a 256-atom programmable quantum simulator. *Nature* **2021**, *595*, 227–232. [CrossRef]
18. Bernien, H.; Schwartz, S.; Keesling, A. Probing many-body dynamics on a 51-atom quantum simulator. *Nature* **2017**, *551*, 227–232. [CrossRef]
19. Das, R.C.; Khan, S.; Ravi, T.; Pandey, K. Direct spectroscopy of Rubidium using a narrow-line transition at 420 nm. *Eur. Phys. J. D* **2024**, *78*, 40. [CrossRef]
20. Urvoy, A.; Carr, C.; Ritter, R.; Adams, C.S.; Weatherill, K.J.; Löw, R. Optical coherences and wavelength mismatch in ladder systems. *J. Phys. B: At. Mol. Opt. Phys.* **2013**, *46*, 245001. [CrossRef]
21. Xu, W.; DeMarco, B. Velocity-selective electromagnetically-induced-transparency measurements of potassium Rydberg states. *Phys. Rev. A* **2016**, *93*, 011801. [CrossRef]
22. Zhu, Y.; Ghosh, S.; ; Cahn, S.B. Electromagnetically-induced-transparency spectroscopy of high-lying Rydberg states in ^{39}K. *Phys. Rev. A* **2022**, *105*, 042808. [CrossRef]
23. Glaser, C.; Karlewski, F.; Kluge, J. Absolute frequency measurement of rubidium $5S-6P$ transitions. *Phys. Rev. A* **2020**, *102*, 012804. [CrossRef]
24. Wu, M.; Bao, X.; Yu, S. Electromagnetically Induced Transparency Spectra of ^{6}Li Rydberg Atoms. *Photonics* **2023**, *10*, 1367. [CrossRef]
25. Li, D.; Bian, G.; Miao, J. Rydberg excitation spectrum of ^{40}K ultracold Fermi gases $5S-6P$ transitions. *Phys. Rev. A* **2021**, *103*, 063305. [CrossRef]
26. Li, B.; Li, M.; Jiang, X.; Qian, J.; Li, X.; Liu, L.; Wang, Y. Optical spectroscopy of nP Rydberg states of ^{87}Rb atoms with a 297-nm ultraviolet laser. *Phys. Rev. A* **2019**, *99*, 042502. [CrossRef]
27. Mack, M.; Karlewski, F.; Hattermann, H. Measurement of absolute transition frequencies of ^{87}Rb to nS and nD Rydberg states by means of electromagnetically induced transparency. *Phys. Rev. A* **2011**, *83*, 052515. [CrossRef]
28. Šibalić, N.; Pritchard, J.D.; Adams, C.S. ARC: An open-source library for calculating properties of alkali Rydberg atoms. *Comput. Phys. Commun.* **2017**, *220*, 319–331. [CrossRef]
29. Li, W.; Mourachko, I.; Noel, M.W. Millimeter-wave spectroscopy of cold Rb Rydberg atoms in a magneto-optical trap: Quantum defects of the ns, np, and nd series. *Phys. Rev. A* **2003**, *67*, 05250. [CrossRef]
30. Han, J.; Jamil, Y.; Noruml, D.V.L. Rb nf quantum defects from millimeter-wave spectroscopy of cold ^{85}Rb Rydberg atoms. *Phys. Rev. A* **2006**, *74*, 054502. [CrossRef]